IEEE Access
Multidisciplinary | Rapid Review | Open Access Journal

Received December 12, 2020, accepted December 22, 2020, date of publication December 25, 2020,
date of current version January 6, 2021.

Digital Object Identifier 10.1109/ACCESS.2020.3047436

Target Localization and Tracking Using an Ultra-Wideband Chaotic Radar With Wireless Synchronization Command

BINGJIE WANG, RUIXIN XIE, HANG XU, JIANGUO ZHANG, HONG HAN, ZHAOXIA ZHANG, LI LIU, AND JINGXIA LI

Key Laboratory of Advanced Transducers and Intelligent Control System, Ministry of Education and Shanxi Province, Taiyuan University of Technology, Taiyuan 030024, China
College of Physics and Optoelectronics, Taiyuan University of Technology, Taiyuan 030024, China

Corresponding author: Hang Xu (xuhang@tyut.edu.cn)

This work was supported in part by the National Natural Science Foundation of China under Grant 61601319, Grant 41704147, and Grant 61805168; in part by the Key Research and Development (R&D) Projects of Shanxi Province under Grant 201803D31037 and Grant 201803D121057 and in part by the Natural Science Foundation of Shanxi Province under Grant 201801D121145 and Grant 201801D221185.

ABSTRACT An ultra-wideband chaotic radar with wireless synchronization command is proposed and experimentally demonstrated for target localization and tracking. This radar uses the wideband chaotic pulse position modulation (CPPM) signal as the probe signal and the radar structure of single-transmitting-dual-receiving. The echo signal scattered from a target is collected by two receivers. The target is located and tracked accurately in two-dimensional space using the signal processing scheme. In particular, the radar receivers can directly generate the CPPM reference signals through a wireless synchronization command, so that the transceivers can be physically separated without cable or optical fiber connection. Experimental results demonstrate the proposed chaotic radar can locate and track the target accurately. A localization error of 11 cm and a detection resolution of 17 cm can be both achieved. Moreover, this radar possesses the excellent immune performance to the external electromagnetic interferences, which makes it suitable in the complex electromagnetic environment caused by the cooperative work of multiple radars.

INDEX TERMS Target localization, target tracking, single-transmitting-dual-receiving radar, chaotic signal, synchronization command.

I. INTRODUCTION

Accurate localization and tracking of targets inside an area are fundamental requirements for security and rescue applications, such as intrusion detection, search and rescue of trapped people, hostage rescue, and soldier reconnaissance. Many technologies, including lidar [1], visual-optical/thermal infrared camera [2], sonar sensor [3], global positioning system (GPS) [4], cellular networks [5], and wireless sensor networks (WSNs) [6] have been proposed for target localization and tracking. However, the lidar and visual-optical/thermal infrared camera are easily disturbed by the temperature and visibility of severe weather, resulting in a large number of false alarms. The sonar sensor is mainly used for underwater target detection, because the attenuation of acoustic waves in water is much less than that in air. The GPS, cellular networks, and WSNs require the targets to share data with the base station via a mobile station, such as a tag in a communication network.

Ultra-wideband (UWB) radar transmits the UWB probe signal into the detection area, and then realizes the localization and tracking of the target by monitoring the target's reflection wave. Compared with other technologies mentioned above, the UWB radar has the following advantages: (1) The electromagnetic wave as the probe signal is not affected by the ambient temperature and visibility, and its attenuation is much less than that of the acoustic wave in the air. (2) The targets as the non-cooperative objects are not equipped with dedicated tags. (3) The wideband frequency characteristic of the UWB radar allows for high range

The associate editor coordinating the review of this manuscript and approving it for publication was Wen-Sheng Zhao.

resolution, good penetration, and simple hardware configuration. The impulse-radio UWB (IR-UWB) radar is a typical UWB radar technology [7]. It uses an impulse signal with a very short duration in the time domain as the probe signal, which occupies a wideband in the frequency domain [8]. Then the position and trajectory of the target can be obtained by analyzing the echo impulse reflected from the target and environment. In addition, the UWB sensor radar networks composed of IR-UWB radars are also proposed for target localization in harsh wireless environments (such as indoor ones) [9], [10] and perimeter protection of critical infrastructures [11], [12], which can operate in monostatic, bistatic, and multistatic modes to create the electromagnetic monitoring area. However, the impulse signal is easily to be affected by the external electromagnetic interferences (EMIs), thus worsening the detection effect. Meanwhile, its repeatable waveform is also recognizable by the intelligent adversary and exposes the user's position [13]. In recent years, UWB noise radar has been developed and demonstrated to overcome the above shortcomings [13]–[16]. Since the transmitted waveform is featureless and wideband, the UWB noise radar possesses several attractive features, such as high range resolution, low probability of detection, and immunity from jamming [14]. It realizes target detection by correlating the noise echo from the target with the reference signal which is the time-delayed replica of the noise probe signal. However, the natural randomness of the noise waveform makes it impossible to control and replicate. Therefore, the reference signal must be transmitted to the receiver by means of cables [15] or optical fibers [16], in the case of transceiver physically separated. However, the cables cannot achieve long-distance transmission, while the optical fiber transmission requires complex and expensive photoelectric conversion devices.

Chaotic signal is characterized with inherent randomness, wide power spectrum, and excellent autocorrelation [17]. Moreover, different from the noise signal, the chaotic signal generated by the deterministic system can be controlled [18] and synchronized [19]. Therefore, the chaotic signal has been used as the radar probe signal [20]–[24]. In 2004, a chaotic radar system using laser chaos was proposed and studied by Lin and Liu for one-dimensional (1D) ranging, and a 9-cm range resolution was demonstrated experimentally [20]. In 2009, a chaos-based UWB radar was presented by Venkatasubramanian *et al.* for through-the-wall imaging application with a resolution of roughly 9 cm [21]. In 2010, a prototype of chaotic signal radar with Colpitts oscillator was set up by Jiang *et al.*, which realized a 12.57-cm range resolution [22]. In 2016, Lin *et al.* applied uncorrelated multichannel chaotic signals generated by electrical heterodyning to multiple-input-multiple-output radar application [23]. In 2019, Xu *et al.* proposed a chaos-based through-wall life-detection radar with a 15-cm range resolution [24]. It has been proved that the chaotic probe signal can achieve the various radar detection functions and high range resolution.

In this paper, the chaotic radar is introduced into target localization and tracking in two-dimensional (2D) space. We propose a wideband chaotic radar with wireless synchronization command. This radar uses the wideband chaotic pulse position modulation (CPPM) signal as the probe signal and the radar structure of single-transmitting-dual-receiving. The target is located and tracked accurately in 2D space using the signal processing scheme. The proposed chaotic radar not only achieves the localization error and detection resolution with centimeter magnitude, but also has the strong anti-EMI performance. In addition, unlike the existing chaotic radars which transmit the reference signal using the cables [25] / optical fibers [26] or generate the reference signal through chaotic synchronization [27], our radar receivers can exactly replicate the CPPM probe signal as the reference signal through a wireless synchronization command. This feature allows the transmitter and receivers to be physically separated without cable or optical fiber connection, which is convenient to expand the detection area.

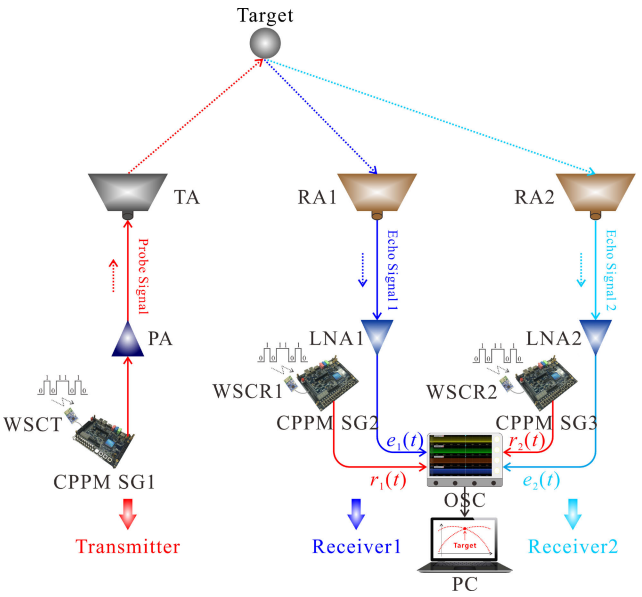

FIGURE 1. Experimental setup of the proposed chaotic radar.

II. EXPERIMENTAL SETUP

Figure 1 gives the experimental setup of the proposed chaotic radar. The wideband CPPM signal is produced by a CPPM signal generator (CPPM SG1) with a wireless synchronous command transmitter (WSCT) and then amplified through a power amplifier (PA). The amplified CPPM signal is transmitted into the detection area utilizing a wideband waveguide double-ridged horn antenna as the transmit antenna (TA). The CPPM echo signal scattered by the target is received by two physically separated receivers. In the receiver1, the echo signal $e_1(t)$ is captured by the receive antenna (RA1) with the same parameters as the TA. The echo signal $e_1(t)$ is amplified by a low noise amplifier (LNA1) and then sent to an OSC for sampling. The CPPM reference signal $r_1(t)$, which is the

replication of the CPPM probe signal, is generated by the CPPM SG2 with a wireless synchronous command receiver 1 (WSCR1) and also sampled by the OSC. The receiver2 has the same structure as the receiver1, including the RA2, LNA2, WSCR2, and CPPM SG3. The echo signal $e_2(t)$ and the reference signal $r_2(t)$ from the receiver2 are also sampled via the OSC. Finally, a personal computer (PC) is utilized to process data and present result. The key component parameters of the proposed chaotic radar are listed in Table 1.

TABLE 1. The key component parameters of the proposed chaotic radar.

Components	Pass-Band/Bandwidth	Other Parameters
PA	75 Hz-10 GHz	Max Gain: 25 dB Gain Step: 5 dB
LNA1, 2	20 MHz-3 GHz	Max Gain: 30 dB Typical Gain: 11 dB
TA, RA1, 2	500 MHz-3 GHz	3dB Beamwidth on E-Plane: 97°-33°
WSCT, WSCR1, 2	2.4 GHz	Sight Distance: 120 m Communication Rate: 0.6-38.4 kbps
OSC	2 GHz	Sampling Rate: 10 GSa/s

III. WIDEBAND CPPM SIGNAL AND WIRELESS SYNCHRONIZATION COMMAND

The CPPM signal is characterized in that the time intervals between adjacent pulses with equal amplitude and width are modulated by a chaos map. It uses the logistic map with a constant initial condition to adjust the pulse interval through a closed-loop feedback structure. The logistic map is written as $x_{m+1} = k(1 - x_m)x_m$ $(m = 0, 1, 2 \ldots\ldots)$, where k is set to 4, and x_0 is selected as 0.4. In this case, although the CPPM signal can be predicted by the above constant initial condition, its pulse intervals still exhibit disorder and aperiodicity, which is used as the radar probe signal to realize the unambiguous ranging. The CPPM SG is realized on a field programmable gate array (FPGA) with 5CGXFC5C6F27C7N model. The specific implementation scheme of the CPPM SG is shown in Fig. 2. Originally, the counter starts to count from zero until the count value exceeds the output value x_{m+1} of the logistic map. Afterwards, the pulse generator is triggered to generate a new pulse. Meanwhile, this pulse is fed back to the input ends of the logistic map and the counter through a closed-loop feedback structure. The rising edge of pulse resets the counter to zero and triggers the logistic map into the update status. The resulting CPPM data streams are stored in the static random access memory (SRAM) via the SRAM controller. The transceiver physical layer (PHY) reset controller releases the reset state of the transceiver PHY. After that, the transceiver PHY generates a feedback clock to the SRAM controller, so that the SRAM controller reads the parallel CPPM data streams from the SRAM and transmits them to the transceiver PHY. Eventually, the transceiver PHY generates the high-speed and wideband CPPM signal after deserializing the parallel data streams.

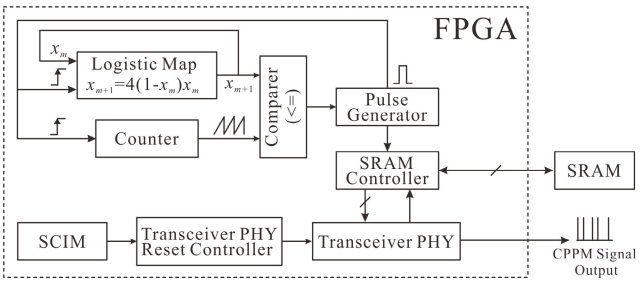

FIGURE 2. Implementation scheme of the CPPM SG.

Based on the synchronous command identification module (SCIM), WSCRs and WSCT with LC12S model, multiple replicated CPPM signals can be output by the CPPM SGs physically separated. Its working principle is as follows: the CPPM SG1 generates the synchronization command (01011010) which is transmitted by the WSCT. After the synchronization command is fully launched, the SG1 generates the CPPM signal. The WSCR1 and WSCR2 firstly receive the 8-bits synchronization command, and then send it to the CPPM SG2/SG3. In SCIMs of the CPPM SG2/SG3, the received command is judged to be consistent with the preset synchronization command by means of temporal logic judgement. If it is consistent, the SCIM will send the set instruction to the transceiver PHT reset controller, and then trigger the CPPM signal output. If not, the WSCR1 and WSCR2 will wait for the next synchronization command. Because all SGs use the same type of FPGA as well as the logistic map with the same k and x_0, the CPPM signals produced by the SG1, SG2, and SG3 should be theoretically identical. The delay time between the CPPM signals generated by the different SGs mainly depends on the judgement time of the received synchronization command in the SCIMs, while the judgement time is determined by the 50-MHz master clock frequency of FPGAs, which is 20 ns. The communication rates of the WSCT and WSCRs are set to 9.6 kbps to achieve a low packet loss rate and provide a long enough holding time for the transmission of a single code within 120-m sight distance, thus eliminating the influence from the transmission time of synchronization command on the delay time between multiple CPPM signals. Based on the WSCT, WSCRs, the same hardware and implementation scheme of CPPM SGs, the CPPM reference signals replicated with the CPPM probe signal can be directly generated in receivers, omitting the use of cables or optical fibers for remote transmission of reference signals between the transceivers. It is beneficial for transceivers separated physically, so as to expand the detection range.

Figure 3 analyzes the features of replicated CPPM signals generated by the SG1, SG2, and SG3. Figures 3(a1)-(a3) plot the temporal waveforms of replicated CPPM signals. The time intervals between adjacent pulses vary randomly according to the logistic map, and the pulse width is 0.64 ns, as magnified in Fig. 3(a1). By comparing the temporal waveforms in Figs. 3(a1)-(a3), it can be found that the CPPM signals generated by three SGs can achieve

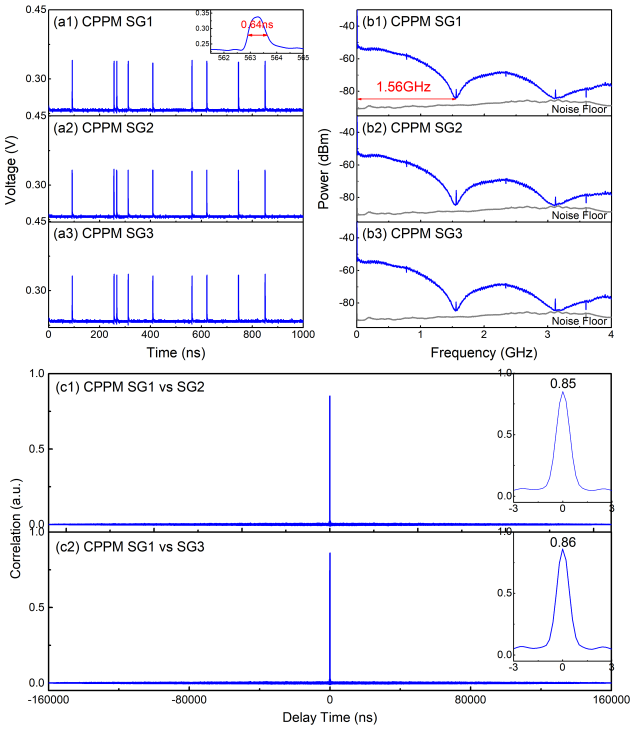

FIGURE 3. **(a) Temporal waveforms, (b) power spectra, and (c) correlation traces of the replicated CPPM signals generated by SG1, SG2, and SG3.**

high synchronization in time domain. The power spectra of replicated CPPM signals are shown in Figs. 3(b1)-(b3), and the bandwidth is 1.56 GHz. They also have the same energy distribution in frequency domain. Figures 3(c1)-(c2) show the correlation traces between the CPPM signals from the SG1 and SG2/SG3, revealing the form of δ-like function. The correlation coefficients between the CPPM signals from the SG1 and SG2/SG3 can reach 0.85 and 0.86, respectively. It is proved that the CPPM signals produced by the SG2/SG3 have a high correlation with the CPPM probe signal produced by the SG1, so they can be used as the reference signals in the receivers. The average power of the CPPM probe signal is 9.10 dBm.

IV. SIGNAL PROCESSING PROCEDURE

In Fig. 4, a signal processing procedure is proposed to realize the accurate localization and tracking of the target in 2D space, which includes the elliptic band-pass filtering (step 1), chaotic correlation ranging (step 2), background subtraction (step 3), and 2D ellipse localization (step 4).

Step 1. Taking the receiver1 as an example, it is assumed that the background echo and reference signal before target detection are $e_{1b}(t)$ and $r_{1b}(t)$ respectively, and the target echo and reference signal after target detection are $e_{1a}(t)$ and $r_{1a}(t)$ respectively. They are processed by the elliptic band-pass filtering to remove high and low frequency interferences, thus generating the filtered echo signals $e'_{1b}(t)$, $e'_{1a}(t)$ and reference signals $r'_{1b}(t)$, $r'_{1a}(t)$. According to the working frequency band of the TA/RAs and the bandwidth

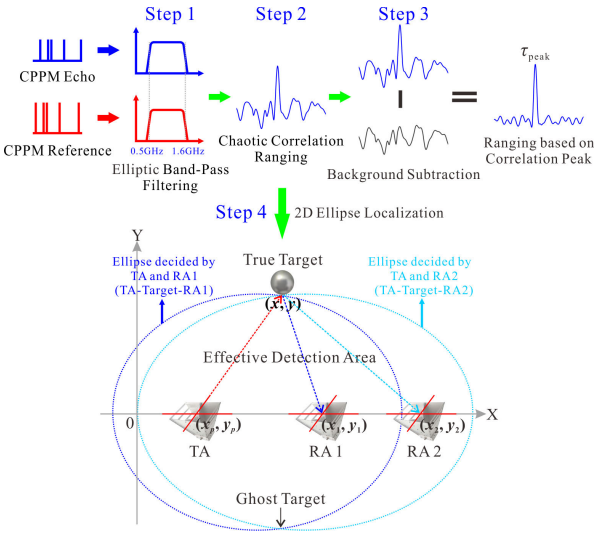

FIGURE 4. **Signal processing procedure of the proposed chaotic radar.**

of CPPM signal, the frequency range of band-pass is set to 0.5 GHz $\sim$ 1.6 GHz.

Step 2. Based on the good autocorrelation characteristic of the CPPM signal, the target distance can be accurately obtained by the narrow and sharp correlation peak. The correlation traces before and after target detection $c_{1b}(\tau_1)$, $c_{1a}(\tau_1)$ are indicated below:

$$c_{1b}(\tau_1) = e'_{1b}(t) \otimes r'_{1b}(t) \tag{1}$$

$$c_{1a}(\tau_1) = e'_{1a}(t) \otimes r'_{1a}(t) \tag{2}$$

where τ_1 is the delay time between the echo signal and reference signal. Note that $c_{1b}(\tau_1)$ and $c_{1a}(\tau_1)$ need to be scaled zero by subtracting the extra delay time from τ_1. The extra delay time includes the transmission time of the CPPM signal on cables, the response time of the CPPM signal on devices, and the delay time of the reference signal in the receiver relative to the probe signal in the transmitter. By docking the transceiver antennas and measuring the delay time based on the correlation peak, the extra delay time is accurately measured with sub-nanosecond accuracy.

Step 3. Through background subtraction, that is, by extracting the difference of correlation traces before and after target detection, the clutter peaks caused by the direct waves from the transmitter and other background clutters can be eliminated. The final ranging trace $c_1(\tau_1)$ is given by:

$$c_1(\tau_1) = c_{1a}(\tau_1) - c_{1b}(\tau_1) \tag{3}$$

If there exists a correlation peak, the TOA of TA-target-RA1 is obtained by the peak position τ_{peak}, and thus the distance d_1 of TA-target-RA1 is equal to $\tau_{\text{peak}} \cdot c$ ($c = 3.0 \times 10^8$m/s). By repeating the above steps, the distance d_2 of TA-target-RA2 can be also obtained.

Step 4. The coordinate system as shown in Fig. 4 is established. Assuming that the aperture center coordinates of TA, RA1, and RA2 marked by the red "X" are (x_p, y_p), (x_1, y_1),

and (x_2, y_2) respectively, the 2D ellipse localization equations for solving the unknown position of the target (x, y) are shown below:

$$\begin{cases} \sqrt{(x-x_p)^2+(y-y_p)^2}+\sqrt{(x-x_1)^2+(y-y_1)^2}=d_1 \\ \sqrt{(x-x_p)^2+(y-y_p)^2}+\sqrt{(x-x_2)^2+(y-y_2)^2}=d_2 \end{cases} \quad (4)$$

where (x_p, y_p), (x_1, y_1), and (x_2, y_2) can be measured by a scaleplate before target detection. By solving Eqs. (4), the target position (x, y) can be obtained. The least-square calculation is applied to solve the equations to obtain the accurate position information.

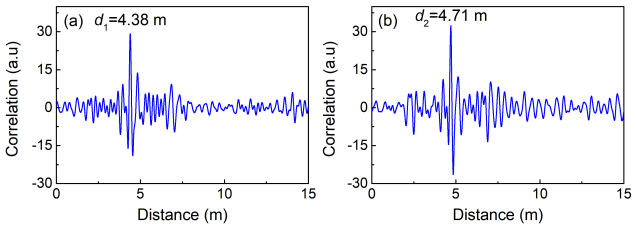

FIGURE 5. (a) Distance d_1 of the short-range target measured by the receiver1, and (b) the corresponding distance d_2 from the receiver2.

V. EXPERIMENTAL RESULTS

A. SINGLE TARGET LOCALIZATION AND TRACKING

Figure 5 shows the ranging results of a static target which is a metal sphere with 28-cm diameter. The sphere center of metal sphere and the aperture center of horn antenna are located at the same height. The coordinates of TA, RA1, and RA2 are (0.70, 0) m, (1.60, 0) m, and (2.20, 0) m, respectively. The correlation peaks in Figs. 5 (a) and (b) show that the target distance d_1 measured by the receiver1 is 4.38 m, while the target distance d_2 measured by the receiver2 is 4.71 m. By solving Eqs. (4), the possible target positions detected by our radar are (0.54, 2.06) m and (0.54, -2.06) m. According to the radiation direction of the directional antennas, it can be known that only (0.54, 2.06) m is located in the effective detection area and serves as the measured target position, while (0.54, -2.06) m is the ghost target position. The actual position of metal sphere in the above coordinate system can be obtained by measuring the spherical vertex position with the scaleplate. By comparing the actual position (0.52, 2.08) m with the measured position (0.54, 2.06) m, the localization error is only 3 cm. Figure 6 further shows the ranging results of the target far away from the antennas. The target distances d_1 and d_2 measured by the receivers 1 and 2 are 12.06 m and 11.99 m, respectively. By comparing the actual position (2.70, 5.80) m with the measured position (2.63, 5.83) m, a localization error of 8 cm is obtained. When the detection range exceeds 6 m, the correlation peak representing the target distance will decrease rapidly and finally be submerged in the background noise.

To further investigate the localization error of the proposed chaotic radar, the measurements of fourteen different target positions in 2D plane are performed. As shown in Fig. 7,

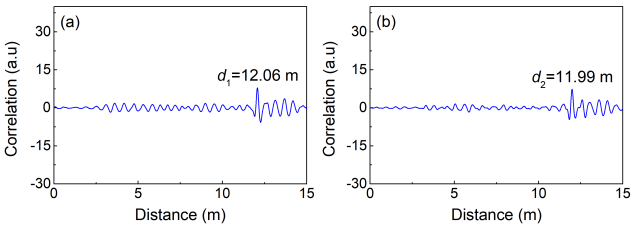

FIGURE 6. (a) Distance d_1 of the long-range target measured by the receiver1, and (b) the corresponding distance d_2 from the receiver2.

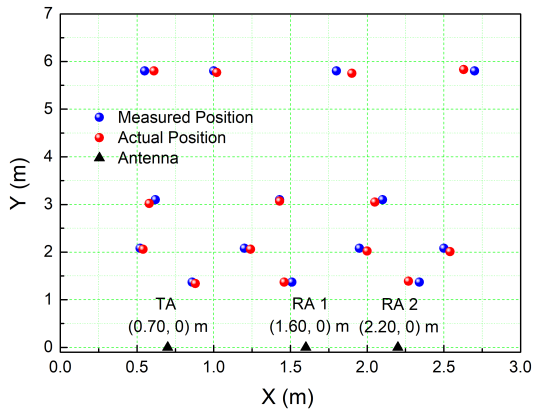

FIGURE 7. Measured positions of fourteen examples and their corresponding actual positions in 2D plane.

TABLE 2. Fourteen examples with measured positions, actual positions, and localization errors.

Example	Measured Position (m)	Actual Position (m)	Error (cm)
1	(0.88, 1.34)	(0.86, 1.37)	4
2	(1.46, 1.37)	(1.51, 1.37)	5
3	(2.27, 1.37)	(2.34, 1.37)	7
4	(0.54, 2.06)	(0.52, 2.08)	3
5	(1.24, 2.06)	(1.20, 2.08)	4
6	(2.00, 2.02)	(1.95, 2.08)	8
7	(2.54, 2.01)	(2.50, 2.08)	8
8	(0.58, 3.02)	(0.62, 3.10)	9
9	(1.43, 3.07)	(1.43, 3.10)	3
10	(2.05, 3.05)	(2.10, 3.10)	7
11	(0.61, 5.80)	(0.55, 5.80)	6
12	(1.02, 5.77)	(1.00, 5.80)	4
13	(1.90, 5.75)	(1.80, 5.80)	11
14	(2.63, 5.83)	(2.70, 5.80)	8

the measured target positions (blue points) given by the proposed radar are consistent with the actual target positions (red points). Table 2 further lists the measured positions, actual positions, and localization errors. It can be found that due to the wideband characteristic of the CPPM signal, the localization error range is from 3 cm to 11 cm within the detection range of 6 m.

When the target moves continuously in the detection area, the OSC in the receiver starts the continuous sampling and storage mode of multi-channel signals. Therefore, the CPPM echo and reference signals at different positions of the target

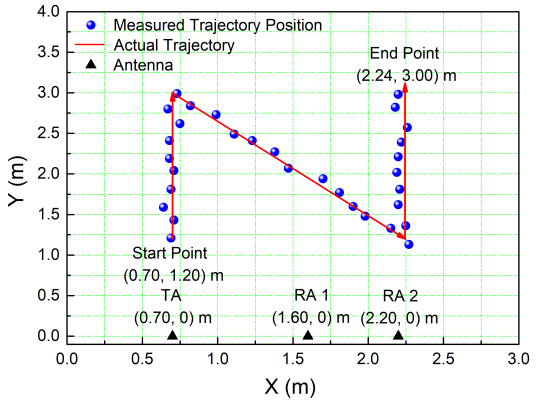

FIGURE 8. Tracking results of a single target in 2D plane.

can be recorded successfully. In Fig. 8, the tracking results of the target in 2D plane are presented, where the blue points are the measured trajectory positions and the red lines indicate the actual trajectory. It can be seen from Fig. 8 that the target moved from the start point (0.70, 1.20) m to the end point (2.24, 3.00) m through a Z-shaped route. As our expected, the measured trajectory positions are almost the same with the actual trajectory, indicating that our radar can detect the target trajectory accurately.

B. TWO TARGET LOCALIZATION AND TRACKING

The proposed chaotic radar also has the ability to locate and track two targets simultaneously. Figure 9 shows the ranging results of two targets. As shown by the two correlation peaks in Fig. 9(a), the two target distances measured by the receiver1 are d_1=3.24 m and d_2=6.23 m, respectively. While the two target distances measured by the receiver2 are d_3=3.61 m and d_4=6.44 m, as plotted in Fig. 9(b). Assuming that the positions of two targets are (x, y) and (x', y'), two equation sets for 2D ellipse localization, each including four equations, can be achieved:

$$\begin{cases} \sqrt{(x-x_p)^2+(y-y_p)^2}+\sqrt{(x-x_1)^2+(y-y_1)^2}=d_1 \\ \sqrt{(x'-x_p)^2+(y'-y_p)^2}+\sqrt{(x'-x_2)^2+(y'-y_2)^2}=d_2 \\ \sqrt{(x-x_p)^2+(y-y_p)^2}+\sqrt{(x-x_1)^2+(y-y_1)^2}=d_3 \\ \sqrt{(x'-x_p)^2+(y'-y_p)^2}+\sqrt{(x'-x_2)^2+(y'-y_2)^2}=d_4 \end{cases} \tag{5}$$

$$\begin{cases} \sqrt{(x-x_p)^2+(y-y_p)^2}+\sqrt{(x-x_1)^2+(y-y_1)^2}=d_1 \\ \sqrt{(x'-x_p)^2+(y'-y_p)^2}+\sqrt{(x'-x_2)^2+(y'-y_2)^2}=d_2 \\ \sqrt{(x-x_p)^2+(y-y_p)^2}+\sqrt{(x-x_1)^2+(y-y_1)^2}=d_4 \\ \sqrt{(x'-x_p)^2+(y'-y_p)^2}+\sqrt{(x'-x_2)^2+(y'-y_2)^2}=d_3 \end{cases} \tag{6}$$

Eqs. (5) have two unique solutions in the effective detection area, which are (0.71, 1.50) m and (0.75, 3.06) m respectively. While Eqs. (6) have no solution, this is because in the triangle formed by the RA1, target1, and RA2, the difference between the distance of RA1-target1 and the distance of RA2-target1

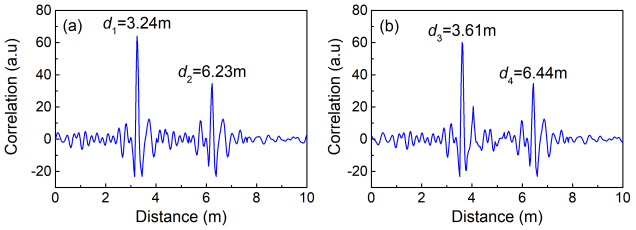

FIGURE 9. (a) Target distances d_1 and d_2 measured by the receiver1, and (b) target distances d_3 and d_4 measured by the receiver2.

($|d_4-d_1|$=3.2 m) is larger than the distance of RA1-RA2 (x_2-x_1=0.6 m), which violates the triangular trilateral relation theorem [28] and makes the equations for target1 in Eqs. (6) unsolvable. Similarly, the equations for target2 in Eqs. (6) also have no solution. Therefore, the two target positions are detected as (0.71, 1.50) m and (0.75, 3.06) m, and the corresponding localization errors are 3 cm and 5 cm, respectively.

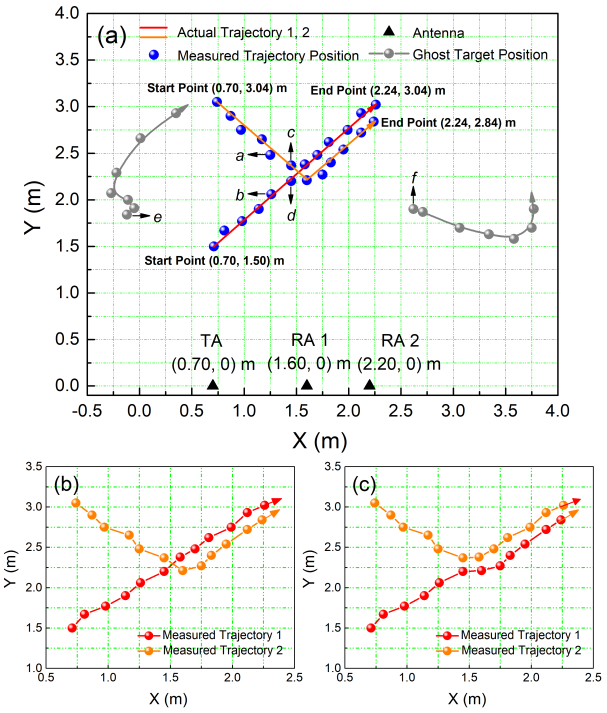

FIGURE 10. (a) Tracking results of two targets in 2D plane. (b) (c) Two possible tracking results.

In Fig. 10, the tracking results of two targets in 2D plane are demonstrated, where the blue/gray points are the measured trajectory positions and the red/orange lines indicate the actual trajectories. As shown in Fig. 10(a), the two targets start from the start points (0.70, 3.04) m and (0.70, 1.50) m respectively, and arrive at the end points (2.24, 3.04) m and (2.24, 2.84) m along different paths. It should be noted that the ghost position elimination and the target matching method need to be further explained. When the distance between the two targets is close, both of Eqs. (5) and (6) have solutions, indicating that in addition to the actual target

positions plotted by the blue points, there exist the ghost target positions shown by the gray points in Fig. 10. These ghost positions can be eliminated according to large distance spans and obvious discontinuities between the ghost positions and the previously measured positions [29]. For example, at time t_0, the measured positions of two targets are points a and b respectively, and there is no ghost position. At the next moment t_1, the measured positions of two targets are points c, d, e, and f. Compared with points c and d, there exist large distance spans and obvious discontinuities between points a and e (a and f), as well as points b and e (b and f) in a very short time. Hence, it can be judged that points e and f are the ghost positions. By analogy, the ghost target positions shown by the gray points can be eliminated. On this basis, two possible tracking results can be obtained as shown in Figs. 10 (b) and (c). In addition, when the trajectories of two targets are very close, the matching problem between targets and trajectories should also be considered. It has been proved that the larger the target's physical size bringing in the stronger reflection signal, which leads to a higher correlation peak [30]. Therefore, in the case of obvious difference in the physical sizes of multiple targets, the targets and corresponding trajectories can be exactly matched by the correlation peak height. If multiple targets have a similar physical size, kurtosis reflecting the motion characteristic of the target can also be used to match targets and trajectories [31]. The energy distribution of the target that repeats the same motion has low kurtosis, while the energy distribution which has less regular motion and significant change instantly has higher kurtosis. Therefore, the above results and analyses prove our radar can track two targets simultaneously, and has the potential to accurately match targets and trajectories.

In general, the detection resolution is calculated as $c/2B$ ($c = 3.0 \times 10^8$ m/s), which mainly depends on the bandwidth B of probe signal. Therefore, a detection resolution of 10 cm can be achieved by taking advantage of the 1.56-GHz full bandwidth of the CPPM signal. In fact, since the working frequency range of TA and RAs is from 500 MHz to 3 GHz, the actual transmission bandwidth of the CPPM signal is 1 GHz, and the corresponding resolution is 15 cm theoretically. In order to verify this resolution, two adjacent metal spheres with 15-cm diameter are used as targets. As shown in Fig. 11, two correlation peaks with a 17-cm spacing are obtained, which is very close to the theoretical resolution of 15 cm. Finally, a 17-cm detection resolution is proved experimentally.

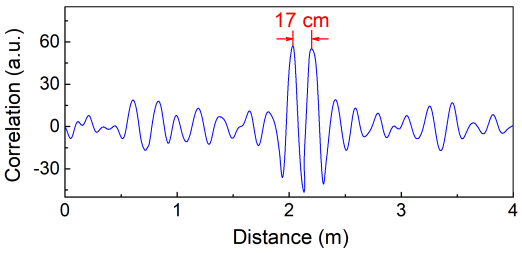

FIGURE 11. Experimental detection resolution of 17 cm.

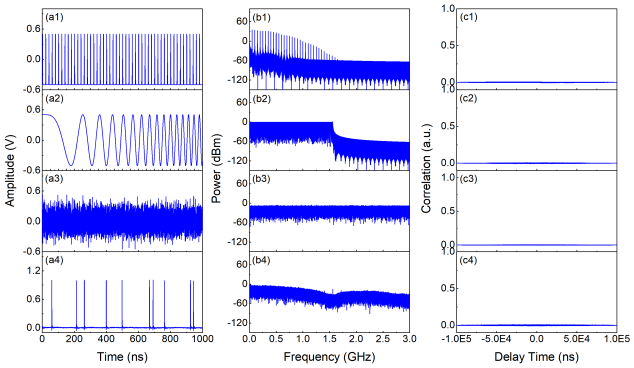

FIGURE 12. (a1)-(a4) Temporal waveforms and (b1)-(b4) power spectra of the impulse, LFMCW, noise, and uncorrelated CPPM signal. (c1)-(c4) Correlation traces between the CPPM reference signal and various interference signals.

C. ANTI-EMI PERFORMANCE

In order to eliminate the detection blind area and reduce the false alarm rate, multiple radars are usually required to cooperative work. Hence, there exist a lot of interferences from the probe signals of other radars such as the IR-UWB radar and linear-frequency-modulated continuous-wave (LFMCW) radar, and the spatial noise in the detection space. The resulting complex electromagnetic environment puts forward high requirements for the radar's anti-EMI performance. One significant feature of our radar is that it has stronger anti-EMI performance compared with the IR-UWB radar. This is because the CPPM signal shows the excellent autocorrelation characteristic as the noise signal. Here the anti-EMI performance of our radar is further analyzed and proved. The influence of interference signals on ranging result is analyzed by superposing the interference signals with different amplitudes on the CPPM echo signal. Figures 12(a1)-(a4) show the temporal waveforms of interference signals such as the impulse, LFMCW, noise, and uncorrelated CPPM signal. It should be explained that the uncorrelated CPPM signal is generated by the logistic map with the initial condition different from our radar, which simulates the probe signal from another chaotic radar. The power spectra of interference signals are plotted in Figs. 12(b1)-(b4). Except that the noise signal has a very wide power spectrum, the cut-off frequency of the other interference signals is 1.56 GHz, which is consistent with the frequency range of CPPM signal. In Figs. 12(c1)-(c4), the correlation traces demonstrate the correlation between the CPPM reference signal and various interference signals is close to zero.

Firstly, the interference-to-signal ratio (ISR) is used to quantify the introduction strengths of interference signals, and its expression is as follows:

$$\mathrm{ISR}=10 \times \log_{10}\left(\sigma / \mu\right) \tag{7}$$

where σ denotes the standard deviation of the interference signal's amplitude, and μ denotes the mean value of the CPPM echo amplitude without interference signals.

Secondly, the peak noise ratio (PNR) of correlation trace is utilized to evaluate the influence of interference signals on ranging result, and its expression is shown as:

$$\mathrm{PNR} = 10 \times \log_{10}\left(\frac{p}{\bar{n} + 3 \times \mathrm{std}\,(n)}\right) \tag{8}$$

where p and n mean the peak value and background noise of the correlation trace, respectively. Figure 13(a) gives the variation curves of PNR as the ISR increases. The results show that the PNR decreases slowly with the increase of ISR for four interference signals. Among them, the PNR of the impulse interference decreases fastest, which indicates that our radar has relatively weak resistance to the impulse interference. Therefore, when the PNR reduces to the 3 dB, the ISR under the impulse interference is served as the tolerance threshold of anti-EMI for our radar, which is 25 dB. At this time, the correlation peak has been submerged in the background noise of the correlation trace and cannot display the target distance, which is a critical case of correlation ranging. Figures 13(b1)-(b4) show the ranging comparison results with or without interference signals when the ISR reaches 20.3 dB. The results show that even if the ISR is as high as 20.3 dB, the position and height of the correlation peak representing the target distance are not affected by interference signals. Therefore, the 2D spatial position of the target is also not disturbed. The above results show that the proposed radar using CPPM signal has the strong anti-EMI performance and can realize the anti-jamming target localization in the complex electromagnetic environment.

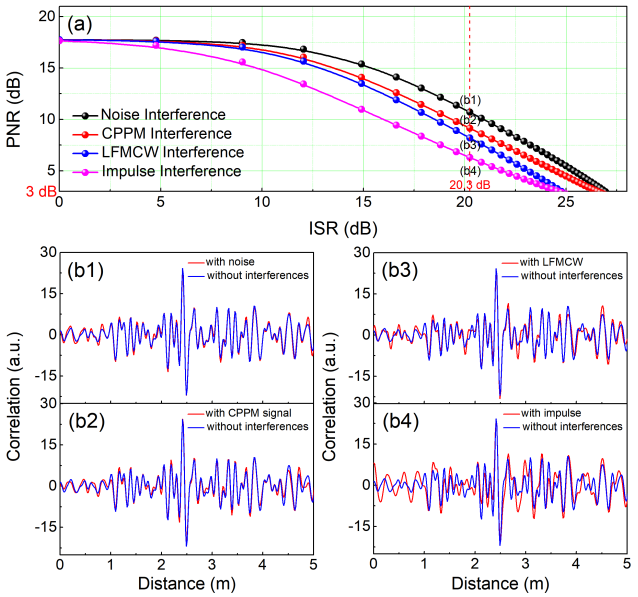

FIGURE 13. (a) Variation curves of PNR as the ISR increases for four interference signals. (b1)-(b4) Ranging comparison results with or without various interference signals when the ISR is 20.3 dB.

VI. DISCUSSION

In the experiment, the proposed chaotic radar locates and tracks one or two targets. If more than two targets appear in the detection area simultaneously, more ghost positions will appear and need to be excluded. By simply increasing the number of transceivers, which can increase the number of localization equations, the ghost positions can be eliminated. Besides, some localization methods of multiple targets for the single-transmitting-dual-receiving radar have also been proposed. In Ref. [31], the matching methods for multi-targets based on the energy and the kurtosis depending on the characteristics of targets have been demonstrated by experiments. In Ref. [32], a pixel-based localization technique using constant false alarm rate detector has been proposed for multiple target cases. Therefore, utilizing the above methods, our radar has the potential to realize the unambiguous detection of multiple targets.

VII. CONCLUSION

In summary, we propose and experimentally demonstrate an UWB chaotic radar with wireless synchronization command for target localization and tracking. The wideband CPPM signal as the probe signal is transmitted and received through one transmitter and two receivers. The target is located and tracked accurately using the signal processing scheme. Experimental results demonstrate the proposed chaotic radar can locate and track the target with low localization error and high detection resolution. Compared with the existing radar systems for target localization and tracking, the unique advantages of our radar are as follows: (1) Benefiting from the wide frequency band and superior autocorrelation characteristics of the CPPM signal, this radar not only realizes the localization error and detection resolution with centimeter-scale, but also has the excellent anti-EMI capability. (2) Based on the wireless synchronization command, the transmitter and receivers are physically separated without cable or optical fiber connection, which is convenient to expand the detection area. In addition, the wideband CPPM signal is easily generated with simpler structure, lower cost, and easier to control than other probe signals. This work provides a promising radar system for safety defense of important and confidential sites.

REFERENCES

[1] K. Wenzl, H. Ruser, and C. Kargel, "Performance evaluation of a decentralized multitarget-tracking algorithm using a LIDAR sensor network with stationary beams," *IEEE Trans. Instrum. Meas.*, vol. 62, no. 5, pp. 1174–1182, May 2013.

[2] M. Teutsch, T. Müeller, M. Huber, and J. Beyerer, "Low resolution person detection with a moving thermal infrared camera by hot spot classification," in *Proc. IEEE Conf. Comput. Vis. Pattern Recognit. Workshops*, Columbus, OH, USA, Jun. 2014, pp. 209–216.

[3] S. Kim, B. Ku, W. Hong, and H. Ko, "Performance comparison of target localization for active sonar systems," *IEEE Trans. Aerosp. Electron. Syst.*, vol. 44, no. 4, pp. 1371–1380, Oct. 2008.

[4] R. Bajaj, S. L. Ranaweera, and D. P. Agrawal, "GPS: Location-tracking technology," *Computer*, vol. 35, no. 4, pp. 92–94, 2002.

[5] R. S. Campos, "Evolution of positioning techniques in cellular networks, from 2G to 4G," *Wireless Commun. Mobile Comput.*, vol. 2017, pp. 1–17, 2017.

[6] T. J. S. Chowdhury, C. Elkin, V. Devabhaktuni, D. B. Rawat, and J. Oluoch, "Advances on localization techniques for wireless sensor networks: A survey," *Comput. Netw.*, vol. 110, pp. 284–305, Dec. 2016.

[7] J. D. Taylor, *Advanced Ultrawideband Radar: Signals, Targets, and Applications*. Boca Raton, FL, USA: CRC Press, 2016.
[8] J. W. Choi, D. H. Yim, and S. H. Cho, "People counting based on an IR-UWB radar sensor," *IEEE Sensors J.*, vol. 17, no. 17, pp. 5717–5727, Sep. 2017.
[9] S. Bartoletti, A. Giorgetti, M. Z. Win, and A. Conti, "Blind selection of representative observations for sensor radar networks," *IEEE Trans. Veh. Technol.*, vol. 64, no. 4, pp. 1388–1400, Apr. 2015.
[10] M. Chiani, A. Giorgetti, and E. Paolini, "Sensor radar for object tracking," *Proc. IEEE*, vol. 106, no. 6, pp. 1022–1041, Jun. 2018.
[11] P. Withington, H. Fluhler, and S. Nag, "Enhancing homeland security with advanced UWB sensors," *IEEE Microw. Mag.*, vol. 4, no. 3, pp. 51–58, Sep. 2003.
[12] H. Mahler and B. Flynn, "Perimeter security intruder tracking and classification using an array of low cost ultra-wideband (UWB) radars," in *Proc. IEEE Int. Symp. Technol. Homeland Secur. (HST)*, Waltham, MA, USA, Apr. 2015, pp. 1–6.
[13] C.-P. Lai and R. M. Narayanan, "Ultrawideband random noise radar design for through-wall surveillance," *IEEE Trans. Aerosp. Electron. Syst.*, vol. 46, no. 4, pp. 1716–1730, Oct. 2010.
[14] R. M. Narayanan, "Through-wall radar imaging using UWB noise waveforms," *J. Franklin Inst.*, vol. 345, no. 6, pp. 659–678, Sep. 2008.
[15] P.-H. Chen, M. C. Shastry, C.-P. Lai, and R. M. Narayanan, "A portable real-time digital noise radar system for through-the-wall imaging," *IEEE Trans. Geosci. Remote Sens.*, vol. 50, no. 10, pp. 4123–4134, Oct. 2012.
[16] D. Grodensky, D. Kravitz, and A. Zadok, "Ultra-wideband microwave-photonic noise radar based on optical waveform generation," *IEEE Photon. Technol. Lett.*, vol. 24, no. 10, pp. 839–841, May 2012.
[17] A. B. Wang, B. J. Wang, L. Li, Y. C. Wang, and K. A. Shore, "Optical heterodyne generation of high-dimensional and broadband white chaos," *IEEE J. Sel. Topics Quantum Electron.*, vol. 21, no. 6, pp. 531–540, Nov. 2015.
[18] W. L. Ditto, S. N. Rauseo, and M. L. Spano, "Experimental control of chaos," *Phys. Rev. Lett.*, vol. 65, no. 26, pp. 3211–3214, Dec. 1990.
[19] L. M. Pecora and T. L. Carroll, "Synchronization in chaotic systems," *Phys. Rev. Lett.*, vol. 64, no. 8, pp. 821–824, Feb. 1990.
[20] F.-Y. Lin and J.-M. Liu, "Chaotic radar using nonlinear laser dynamics," *IEEE J. Quantum Electron.*, vol. 40, no. 6, pp. 815–820, Jun. 2004.
[21] V. Venkatasubramanian, H. Leung, and X. X. Liu, "Chaos UWB radar for through-the-wall imaging," *IEEE Trans. Image Process.*, vol. 18, no. 6, pp. 1255–1265, Jun. 2009.
[22] T. Jiang, J. Long, Z. Wang, S. Qiao, W. Cui, W. Ma, J. Huangfu, and L. Ran, "Experimental investigation of a direct chaotic signal radar with colpitts oscillator," *J. Electromagn. Waves Appl.*, vol. 24, nos. 8–9, pp. 1229–1239, Jan. 2010.
[23] C.-H. Cheng, Y.-C. Chen, and F.-Y. Lin, "Generation of uncorrelated multichannel chaos by electrical heterodyning for multiple-input-multiple-output chaos radar application," *IEEE Photon. J.*, vol. 8, no. 1, Feb. 2016, Art. no. 7800209.
[24] H. Xu, L. Q. Li, Y. Li, J. G. Zhang, H. Han, L. Liu, and J. X. Li, "Chaos-based through-wall life-detection radar," *Int. J. Bifurcation Chaos*, vol. 29, no. 7, Jun. 2019, Art. no. 1930020.
[25] B. J. Wang, H. Xu, P. Yang, L. Liu, and J. X. Li, "Target detection and ranging through lossy media using chaotic radar," *Entropy*, vol. 17, no. 4, pp. 2082–2093, Apr. 2015.
[26] H. Xu, B. J. Wang, H. Han, L. Liu, J. X. Li, Y. C. Wang, and A. B. Wang, "Remote imaging radar with ultra-wideband chaotic signals over fiber links," *Int. J. Bifurcation Chaos*, vol. 25, no. 11, Oct. 2015, Art. no. 1530029.
[27] C. S. Pappu, B. C. Flores, P. S. Debroux, and J. E. Boehm, "An electronic implementation of lorenz chaotic oscillator synchronization for bistatic radar applications," *IEEE Trans. Aerosp. Electron. Syst.*, vol. 53, no. 4, pp. 2001–2013, Aug. 2017.
[28] J. Rovňáková and D. Kocur, "TOA estimation and data association for through-wall tracking of moving targets," *EURASIP J. Wireless Commun. Netw.*, vol. 2010, no. 1, Aug. 2010, Art. no. 420767.
[29] X. L. Chen, H. Leung, and M. Tian, "Multitarget detection and tracking for through-the-wall radars," *IEEE Trans. Aerosp. Electron. Syst.*, vol. 50, no. 2, pp. 1403–1415, Apr. 2014.
[30] H. Xu, R. X. Xie, H. Han, Z. X. Zhang, J. G. Zhang, L. Liu, B. J. Wang, and L. Q. Li, "A LCX-based intrusion-detection sensor using a broadband noise signal," *IEEE Access*, vol. 7, pp. 161928–161936, Nov. 2019.
[31] D.-H. Kim, D.-W. Lim, L. Shen, H.-M. Kim, S.-C. Woo, and H. K. Yu, "Localization methods of multi-targets for UWB radar sensor networks," in *Proc. 3rd Int. Asia–Pacific Conf. Synth. Aperture Radar (APSAR)*, Seoul, South Korea, Sep. 2011, pp. 1–4.
[32] B. Sobhani, M. Mazzotti, E. Paolini, A. Giorgetti, and M. Chiani, "Multiple target detection and localization in UWB multistatic radars," in *Proc. IEEE Int. Conf. Ultra-WideBand (ICUWB)*, Paris, France, Sep. 2014, pp. 135–140.

BINGJIE WANG received the Ph.D. degree in circuit and system from the Taiyuan University of Technology, China, in 2012. She is currently an Associate Professor with the Key Laboratory of Advanced Transducers and Intelligent Control System, Ministry of Education and Shanxi Province, Taiyuan University of Technology. Her research interests include the laser radar and time-domain reflectometry.

RUIXIN XIE received the B.Eng. degree from the Hunan University of Science and Technology, China, in 2017. He is currently pursuing the M.Eng. degree with the Taiyuan University of Technology. His research interest includes intrusion detection sensor.

HANG XU received the Ph.D. degree in physical electronics from the Taiyuan University of Technology, China, in 2015. He is currently an Associate Professor with the Key Laboratory of Advanced Transducers and Intelligent Control System, Ministry of Education and Shanxi Province, Taiyuan University of Technology. His research interests include through-wall imaging radar, life-detection radar, and intrusion detection sensor.

JIANGUO ZHANG received the Ph.D. degree in circuit and system from the Taiyuan University of Technology, China, in 2013. He is currently an Associate Professor with the Key Laboratory of Advanced Transducers and Intelligent Control System, Ministry of Education and Shanxi Province, Taiyuan University of Technology. His research interest includes microwave photon radar.

HONG HAN received the Ph.D. degree in optics from the Harbin Institute of Technology, China, in 2014. She is currently an Associate Professor with the Key Laboratory of Advanced Transducers and Intelligent Control System, Ministry of Education and Shanxi Province, Taiyuan University of Technology. Her research interests include the dynamic features of chaotic lasers and chaotic security communication.

ZHAOXIA ZHANG received the Ph.D. degree in circuit and system from the Taiyuan University of Technology, China, in 2010. She is currently a Professor with the College of Physics and Optoelectronics, Taiyuan University of Technology. Her research interests include through-wall imaging radar, life-detection radar, and cognitive radar.

LI LIU received the Ph.D. degree in physical electronics from the Beihang University, China, in 2011. She is currently an Associate Professor with the Key Laboratory of Advanced Transducers and Intelligent Control System, Ministry of Education and Shanxi Province, Taiyuan University of Technology. Her research interests include the through-wall imaging radar, life-detection radar, and ground penetrating radar.

JINGXIA LI received the Ph.D. degree in circuit and system from the Taiyuan University of Technology, China, in 2013. She is currently an Associate Professor with the Key Laboratory of Advanced Transducers and Intelligent Control System, Ministry of Education and Shanxi Province, Taiyuan University of Technology. Her research interests include ultra-wideband random signal generation and ground penetrating radar.